Lab on a Chip

PAPER

Cite this: *Lab Chip*, 2016, **16**, 2487

Confinement of water droplets on rectangular micro/nano-arrayed surfaces†

Ondřej Kašpar,‡[a] Hailong Zhang,‡[b] Viola Tokárová,[a] Reinhard I. Boysen,[b] Gemma Rius Suñé,[c] Xavier Borrise,[c] Francesco Perez-Murano,[c] Milton T. W. Hearn[b] and Dan V. Nicolau*[ab]

Received 12th May 2016,
Accepted 27th May 2016

DOI: 10.1039/c6lc00622a

www.rsc.org/loc

Micro-patterned surfaces with alternate hydrophilic and hydrophobic rectangular areas effectively confine water droplets down to attolitre volumes. The contact angle, volume, and geometry of the confined droplets as a function of the geometry and physico-chemical properties of the confining surfaces have been determined by phenomenological simulations, validated by atomic force microscopy measurements. The combination between experiments and simulations can be used for the purposeful design of arrays with surface-addressable hydrophobicity employed in digital microfluidics and high-throughput screening nanoarrays.

Introduction

The wettability of surfaces presenting micro- and nano-scale geometrical patterns is a phenomenon which is essential for the operation of many biomedical microdevices,[1] *e.g.*, microarrays,[2–5] lab-on-a-chip,[6,7] digital microfluidics,[8–11] and biosensors,[12–14] as well as myriads of natural biological systems, *e.g.*, shark[15] and gecko skin,[16] insect wings,[17,18] and lotus leaves.[19,20] This ubiquity and its importance have led to early and constant efforts focused on the understanding of wetting on micro- and nano-structured surfaces. Indeed, the basic principles of the wetting of topographically and chemically heterogeneous surfaces have been described[21] by the well-known Cassie–Baxter's[22] and Wenzel's[23] laws, respectively. Despite this classical knowledge, many aspects of this process, *e.g.*, the micro/nano-size of the surface features and liquid entities, their various shapes, the large number of instances of contact points, and the connectivity between adjacent fluid volumes, generate complex phenomena.[24] This complexity makes a predictive approach difficult, as even relatively simple surface topographies, *e.g.*, grooves with rectangular cross-sections and identical surface chemistry, exhibit a large variety of different wetting morphologies.[25] Notwithstanding this difficulty, the understanding of the wetting of micro/nano-structured surfaces is becoming more important and imperative, in part due to the advances in micro- and nano-fabrication,[26] including for biological applications,[27] and in part due to the many types of biomedical microdevices that employ purposefully designed micro/nano-structures for the control of wettability.[1] Consequently, many studies in the past decade have used various methodologies, both theoretical and experimental, to understand and predict the behaviour of small volumes of liquid on topographically and chemically heterogeneous surfaces. For instance, theoretical studies used molecular dynamics[28–32] and density functional theory[33,34] to simulate the wetting process, and classical approaches focused on the balance between Laplace pressure and interfacial tensions to predict the free surface of the droplets on micro/nano-topographies. On the experimental front, the wetting has been studied on various purposefully designed topographies[25,35] or flat patterns with different hydrophobicities.[36–39] Additionally, due to the small scale of the systems involved, advanced microscopy techniques, such as interference microscopy, confocal microscopy, environmental scanning electron microscopy, and atomic force microscopy (AFM),[40] were needed to be employed to establish the droplet profile. While AFM is the tool of choice for the visualization of solid micro/nano-topographies, including for studies of the wetting of micro/nano-structures,[25] its use for liquid surfaces is non-trivial, both experimentally[40] and theoretically.[41] It has been demonstrated,[25,42,43] however, that the AFM tapping mode can be used to measure the contact angle of microscopic droplets. This work explores the limits of the capability of ordered, micron-sized patterns, which alternate hydrophobic and hydrophilic areas, to confine water microdroplets on practically flat surfaces. Furthermore, the

[a] *Department of Bioengineering, Faculty of Engineering, McGill University, Montreal, Quebec, H3A 0C3, Canada. E-mail: dan.nicolau@mcgill.ca*
[b] *ARC Special Research Centre for Green Chemistry, School of Chemistry, Monash University, Clayton, VIC 3800, Australia*
[c] *CNM-IMB, Centro Nacional de Microelectronica, CSIC, E-08193 Bellaterra, Spain*
† Electronic supplementary information (ESI) available. See DOI: 10.1039/c6lc00622a
‡ Both authors contributed equally to this work.

This journal is © The Royal Society of Chemistry 2016

comparison between the topographies inferred from AFM scanning and those obtained from simulations offers a methodological blueprint for the design of surfaces that efficiently confine microdroplets intended for a variety of applications, in particular micro- and nano-arrays and open surfaces, or digital microfluidics.

Experimental

Design and fabrication of micro-structured arrays

The micro-structured arrays were manufactured using 1 × 1 cm^2 chips cut from P-doped silicon wafers submitted to a dry thermal oxidation process to form a 40 nm thick SiO_2 layer. The 50 μm × 50 μm patterned areas were defined by e-beam lithography (described in Fig. 1). Briefly, a 100 nm thick layer of a positive e-beam resist (poly-methyl methacrylate, PMMA 950k) was deposited by spin coating on the chip surface, processed by e-beam lithography exposure and development; a 35 nm thick Au-on-Cr (30 nm/5 nm) layer was deposited over the whole chip by e-beam evaporation; the remainder of the PMMA was removed with acetone. The fabrication process results in the formation of oxidized silicon rectangular 'valleys' surrounded by Au surfaces. The structures were finally methyl-terminated thiol-functionalized, leaving the Au (hydrophobic) as an elevated layer.

Deposition of water microdroplets

Of the several methods for the production of micron-sized droplets, *e.g.*, electrospray,[44] droplet emulsions,[45,46] condensation in environmental chambers[47] or ultra-small dispensers based on custom-made AFM hollow cantilevers,[48] spraying is decisively the simplest. The kinetic energy of an expanding gas is used to overcome the surface tension force of the liquid leading to jets that break up into fine droplets.[49] In this study, a nebulizer has been used to produce micro-sized droplets deposited on micro-patterned surfaces. The advantage of this method is the simultaneous deposition of a large number of droplets under identical experimental conditions using a wide range of commercial atomizers (sprays, nebulizers). Its disadvantage is the lack of precise control of droplet size and location.[50] Ultra-pure water (18.2 MΩ cm) was sprayed onto micro-structured surfaces using a commercially available nebulizer, which generates small droplets with a narrow size distribution, *e.g.*, more than 89% droplets with a diameter smaller than 5 μm.[51] This fine-droplet fraction (<5 μm) is best suited for efficient drug delivery to distal airways.[52] In order to prevent evaporation and saturate the surrounding air at room temperature, few large water droplets were applied in the closed ('wet') chamber prior to AFM tapping mode imaging. The humidity was monitored and kept at saturation levels during experimentation.

AFM imaging and surface characterization

The samples were characterized using a PicoPlus AFM (Molecular Imaging Inc., Tempe, AZ, USA), controlled with a Picoscan 3000 controller (Molecular Imaging). All topographic images were acquired in alternating current (AC) mode to reduce the soft surface damage. Ultrasharp silicon probes (NSC15/AIBS, MikroMasch, Madrid, Spain) with a typical spring constant of 40 N m^{-1} were used in tapping mode. AFM imaging was performed in ambient air at 25 °C at a tapping frequency of 300 kHz, near the resonance frequency of the cantilever. The scan field of view was 20 μm × 20 μm using a scanning rate of 1 Hz and 512 scanning lines. The surface topography characterization, cross-section analyses and contact angle determination on structured surfaces were carried out using the software WS-XM 4.0 Develop 10.4.[53] As the space underneath the horizontal circumference of a

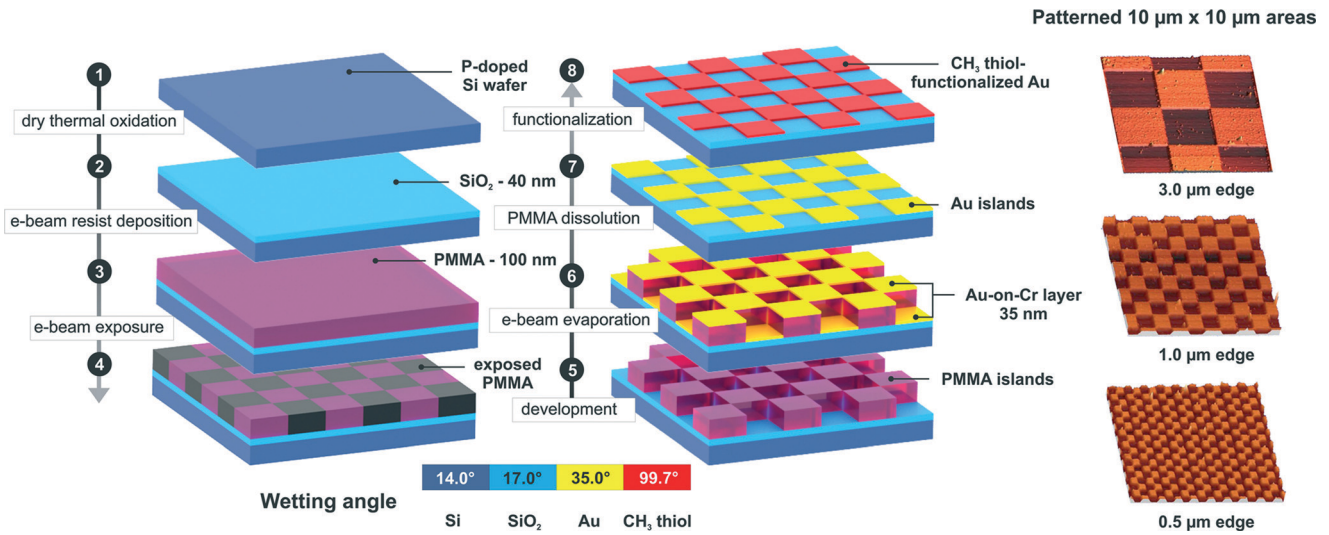

Fig. 1 Patterned surfaces for testing the capacity of confining water droplets. Standard e-beam lithography has been used to generate hydrophilic basal surfaces (SiO_2) surrounded by thin layered materials (Au). Subsequent functionalization of Au with CH_3 thiol resulted in the formation of a chessboard hydrophobic pattern. The inset presents AFM micrographs of the chessboard Au patterns on SiO_2 for three sizes of the confining rectangles. For fabrication details, see also the Experimental section.

 This journal is © The Royal Society of Chemistry 2016

droplet cannot be accessed by AFM, the maximum contact angle that could be measured was 90°.

Contact angle measurements

The static contact angles on reference surfaces, *i.e.*, Si, SiO_2 and Au, both bare and thiol-functionalized, were measured with an OCA 200 contact angle goniometer (Dataphysics Instruments GmbH, Filderstadt, Germany) using the sessile drop technique with 1 μL of nanopure water (18.2 MΩ cm) in air at room temperature (25 °C). The results are presented in the ESI† (Table S1).

Droplet simulations

The shape of the droplet confined in the rectangular wells was simulated using the public domain software Surface Evolver.[54] The Surface Evolver program, extensively used to analyse the fluid interface,[55–57] calculates the shape of a droplet at equilibrium, through the minimization of the free energy of the system. On the micro-scale, the capillary and surface tension forces are predominant compared with gravity. The dimensionless Bond number (Bo) is commonly used to determine the impact of gravity force on the system. If Bo $\ll$ 1, the influence of gravity is negligible.[58] For example, the Bo value for a water microdroplet with 10 μm radius is 1.4×10^{-7}. The parameters of the droplet were water density = 1000 kg m^{-3} and surface tension for water at 25 °C = 0.072 N m^{-1}.[59]

The equilibrium of the droplet shape has been obtained iteratively from the initial shape, *e.g.*, a box, positioned into a fixed model of the well (Fig. S2a†). The process was divided into a series of individual steps to ensure stable simulations (Fig. S2b–d†). After each iteration step, the vertices on the interface were moved to reduce the energy of the system while adhering to a set of imposed constraints. Detailed information about the software, syntaxes and principles is available in the Surface Evolver manual.[60] The contact angle was measured by using a public domain software program, ImageJ,[61] with an implemented plugin that had been designed especially for the drop shape analysis – DropSnake.[62]

The study of the confinement of water microdroplets on micro-structured surfaces used a set of patterns (Fig. 1), which comprise a rectangular array of hydrophilic SiO_2 basal layers (contact angle 17°), surrounded by hydrophobic surfaces, *i.e.*, made of a thin layer of CH_3-terminated thiol-functionalized Au (contact angle 99.7°). The impact of the 'allowed wetting' hydrophilic area on the lateral confinement of droplets has been assessed using chessboard-like hydrophilic patterns with different dimensions, *i.e.*, 3 μm × 3 μm, 1 μm × 1 μm, or 0.5 μm × 0.5 μm rectangles.

Results and discussion

In contrast to other reports,[25,35] which focused on the confinement capacity of structures modulated by the ratio (X) between the height of the vertical walls (h) and the width of the horizontal areas (L) for microstructures made of the same material, our study has focused on the area of 'allowed wetting' of a hydrophilic 'lake' surrounded by a 'wetting-forbidden desert'. Indeed, the height of the walls surrounding the hydrophilic areas and the ratio between this height and the width of the hydrophilic rectangles are very low, *i.e.*, h = 35 nm and X = 0.01–0.07, respectively (compared with X = 0.05–0.60 as reported elsewhere[25]). For these low values, the confinement due solely to the height of the vertical walls, assessed by using structures where the hydrophilic rectangles are surrounded by equally hydrophilic walls, has been shown to be negligible (Fig. SI3a†). Conversely, when the difference between the hydrophobicities of the basal surface and the surrounding wall is high, *i.e.*, ΔCA = 82.7°, the confinement of the water droplets is nearly perfect (Fig. 2a).

The near-perfect confinement (Fig. 2a–c) of the large droplets, on large areas, *i.e.*, 3 μm × 3 μm, which is evident from the absence of any significant spillover, appears to be also preserved for smaller areas, *i.e.*, 1 μm × 1 μm and 0.5 μm × 0.5 μm (Fig. 2b and c, respectively). Furthermore, the dome-like morphology of the droplets is also preserved, regardless of the size of the confining area or the volume of the droplet. If the well is not fully wetted, *i.e.*, the droplet footprint only partially covers the bottom of the well and its rim, the preferential wetting of the hydrophilic bottom drags the liquid into the well, and thus spontaneously rearranges the chaotically deposited droplets into the predetermined patterns, as presented in Fig. 2.

While different droplet volumes will inherently translate at various contact angles, if the droplet makes contact with the edges of the confining areas, the contact angles will also vary along the contact line of the droplet with the surface, reaching a maximum in the middle of the rim and smaller values towards the corners (Fig. SI6a and b and SI7a and b†). The contact angle at the point of contact of the droplet and the middle of the horizontal rim of the well can be estimated both from the AFM measurements and from simulations. This contact angle can reach any value from 9.7° (first contact of droplet with the rim) to 99.7° (for the maximum volume of the confined droplet) (Fig. 3a).

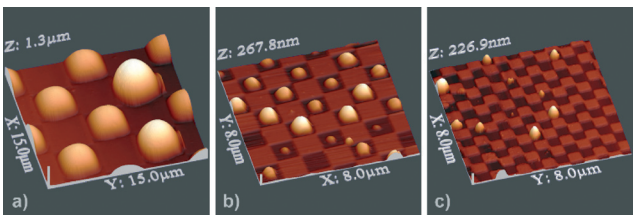

Fig. 2 Nearly perfect confinement, *i.e.*, no spillover, of microdroplets by rectangular hydrophilic patches surrounded by surfaces with high hydrophobicity. Confinement areas: (a) 3 μm × 3 μm, (b) 1 μm × 1 μm, and (c) 0.5 μm × 0.5 μm. The repellent feature of the surrounding hydrophobic walls is stronger for smaller confining areas, *e.g.*, manifested by the central positioning of the microdroplets in smaller confining rectangles, as opposed to microdroplets touching the hydrophobic walls for larger confining areas. Note: the aspect ratio of the Z-axis has been increased to ensure better droplet visibility. The X, Y and Z values represent the range of the measured area.

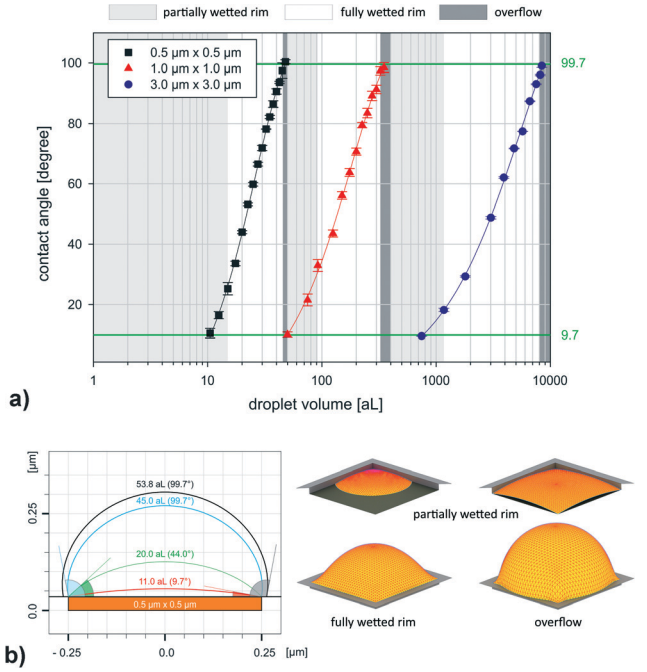

Fig. 3 (a) Dependence of contact angle and the volume of the confined droplets for all three size classes of the well. The contact angle is determined from the perpendicular cross-section of the simulated droplet shape and measured between the droplet and the horizontal rim. The critical transition regions, *i.e.*, when the droplet partially, or fully, wets the rim of the well and when it reaches the maximum and overflows the rim, are labelled in different shades of grey. (b) Left: perpendicular cross-section of droplets in the 0.5 µm × 0.5 µm well (red outline – the first contact with the rim; blue outline – the maximal confinable volume; black outline – droplet overflow); right: equilibrium droplet shape for critical transition regions evaluated by Surface Evolver.

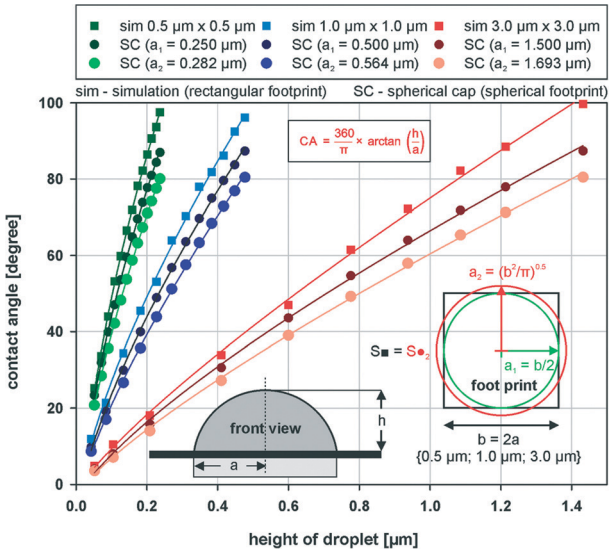

Fig. 4 Contact angle (CA) as a function of droplet height and the comparison of CA values based on the approximation of the droplet shape with a spherical cap (SC) of the same height. The radius of the spherical cap was chosen as either that of a circle inscribed in the rectangular well (a_1) or that of a circle of the same footprint area as the rectangular well (a_2).

The simulation of the 3D profiles of the droplets (Fig. 3b) predicts the maximum volumes above the plane of the rim (*i.e.*, before the droplet 'bursts' and floods the areas outside the well) of 36.25 aL (denominated further as V_{small}), 290 aL ($2^3 \times V_{small}$) and 7.83 fL ($6^3 \times V_{small}$) for the small (0.5 µm × 0.5 µm), medium (1 µm × 1 µm) and large (3 µm × 3 µm) structures, respectively. A more detailed relationship between the droplet volume and the contact angle at the rim is presented in the ESI† (Fig. SI7 and SI8).

The values of the contact angles obtained from phenomenological simulations were then compared with those calculated from an approximation of the shape of the droplet with a spherical cap having the same height. The radius of the spherical cap was chosen as either that of a circle inscribed in the rectangular well (a_1) or that of a circle with the same area as the rectangular well (a_2) (Fig. 4). The contact angles calculated from equivalent spherical cap estimations underestimate the simulated values, by 11% and 20%, for a_1 and a_2 radii, respectively.

The shape of the spherical cap geometry is valid for droplets on flat homogeneous surfaces. Consequently, an analytical relationship that links the maximum volume of the droplet to its footprint surface area, *i.e.*, $V = k \times S_{FP}^{1.5}$, where V is the volume, S_{FP} is the footprint area, and k is a regression coefficient depending solely on the properties of the confining surface, can be derived. Fig. 5 presents these relationships for hydrophilic (SiO_2, CA = 17.0°) and hydrophobic (CH_3-functionalised Au, CA = 99.7°) surfaces. Interestingly, the analysis of the simulated data shows that the mathematical formalism of this relationship is also valid for droplets confined in rectangular shallow wells (Fig. 5). The development of these relationships and the analysis they facilitate lead to several significant outcomes.

First, the unequivocal relationship between the maximum volumes of a droplet on a flat, hydrophobic (*i.e.*, $CA_{hydrophobic}$ = 99.7°) surface and those of a confined droplet in a shallow rectangular well allows the calculation of an 'effective' contact angle. This 'effective' contact angle, estimated to be CA_{eff} = 79.9° (Fig. 5), is the contact angle of a homogeneous surface for a droplet with volume and a footprint area identical to those of a droplet confined in a rectangular well with shallow hydrophobic walls made of a material with a contact angle of 99.7°. The ratio $CA_{hydrophobic}/CA_{eff}$ = 1.25 is valid for all wetting angles where it is physically possible to confine the droplet volume in a rectangular well, *i.e.*, CA of the wall materials must be in the range 45–135°, as predicted by the Concus–Finn relations (ESI† SI3). The 'effective' contact angle provides a quick estimation of the properties of an equivalent hydrophobic flat surface replaced by a patterned one comprising calibrated hydrophilic islands in a more hydrophobic 'sea'.

Second, several contradictory parameters determine the effectiveness of a particular diagnostic, biosensing, or high-throughput screening planar device using small liquid volumes on surfaces. The cost-effectiveness and multiplexing capability demand the smallest possible volumes of the analyte solution. However, the interplay between the sensitivity of detection, *e.g.*, by fluorescence, and the concentration of the chemical species of interest, which are in many instances

 This journal is © The Royal Society of Chemistry 2016

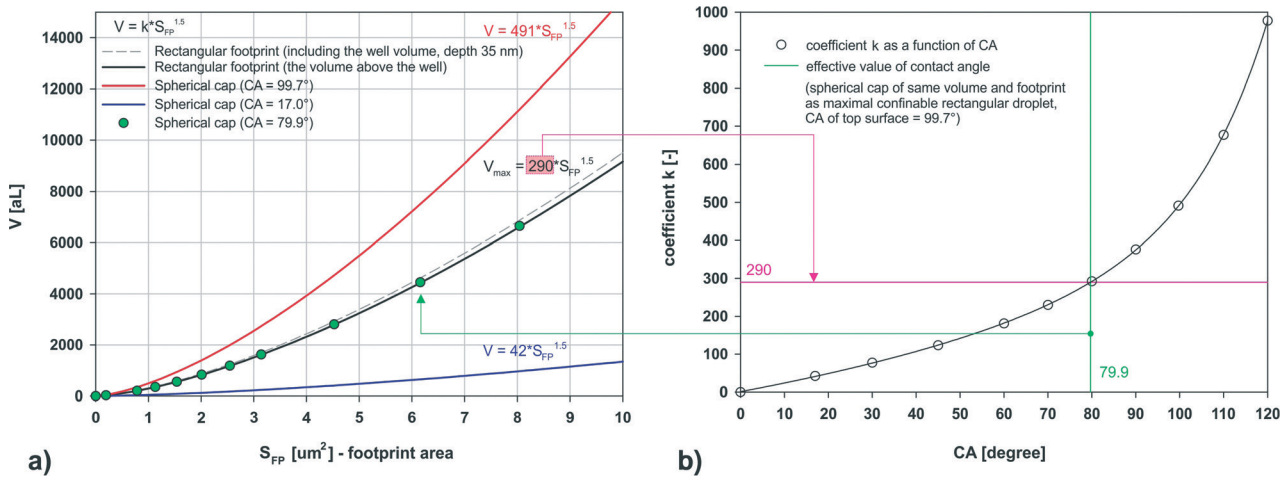

Fig. 5 (a) Maximum confined volume as a function of footprint area (S_{FP}) for the chessboard-like patterned surface/rectangular wells ('rectangular' droplets) and flat homogeneous hydrophilic (17.0°) and hydrophobic (99.7°) surface/spherical wells (spherical cap droplets). (b) Coefficient k as a function of contact angle (CA) for spherical cap. The grey horizontal line represents the coefficient k for rectangular wells (290), and the green vertical line corresponds to the value of the 'effective' contact angle (approx. 79.9°). This value is used for the calculation of the spherical cap volume based on the footprint and 'effective' contact angle – green points in plot a).

given parameters for a particular application, will dictate the minimum volume of a solution of the analyte. More hydrophobic surfaces would allow the 'packing' of greater volumes of liquid droplets on the unit area, thus fulfilling both the requirements of the limit of detection and multiplexing. However, hydrophobic surfaces could induce deleterious effects, *e.g.*, denaturation of surface-adsorbed proteins, and hydrophilic surfaces might be required, *e.g.*, for covalent immobilization of target biomolecules. In this context, the relationship between the droplet volume and footprint area shows that the spherical cap droplet on the flat hydrophobic substrate holds 69% more volume compared to the maximum volume of a droplet confined in a rectangular well with the same footprint area. On the other hand, the spherical cap droplet on the model hydrophilic surface is able to hold 85% less volume compared to a rectangular well of the same footprint. Therefore, using this methodology, one can estimate the cost in 'lost' volume of the droplet for the same multiplexing capability, when replacing a hydrophobic surface with a hydrophilic/hydrophobic chessboard-patterned one, but still avoiding larger losses required by a hydrophilic flat surface.

Third, because the contact angle of the droplet along the edge of the well boundary is not constant, the calculation of the droplet volume requires non-trivial simulations, as presented here. However, the derived semi-empirical relationship allows the estimation of the maximum volume of a droplet confined in a nano/micro square well, *i.e.*, with a non-spherical cap shape, without the need for elaborate simulations or difficult experiments. The simulations have been further used to find a correlation between the contact angle (as defined above) and the height of the droplet above the rim (Fig. SI9†). Because AFM measurements are problematic at the intersection of two types of surfaces, *i.e.*, hydrophobic-functionalized Au and water, the height of the confined microdroplets measured by AFM was chosen as the most reliable parameter for the estimation of the contact angle (by a correlation described in the ESI†). The contact angles determined from experimental AFM data correlate well with those obtained from the simulations using the AFM-measured heights (Fig. 6). This methodology, which can be extended to other geometries of the shallow wells, *e.g.*, channels, half-circles, *etc.*, can be used for the rapid design of patterned surfaces that manage wettability at the micron level for, *e.g.*, microarrays and digital microfluidics.

Fourth, the stability of a droplet in a well, when gravity force is negligible, is classically described by Concus–Finn relations,[63] derived for the self-capillary motion and de-wetting in the corner of the well.[64] If θ is the contact angle on a flat surface made of the same material as the vertical walls (here 99.7°), and α is the angle between two vertical plane walls, then the condition for capillary self-motion is $\theta < (\pi - \alpha)/2$ and that

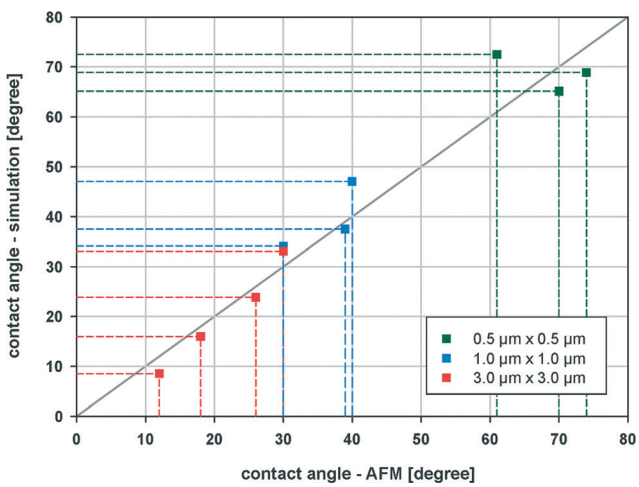

Fig. 6 CA values for the confined microdroplets determined by AFM *vs.* those obtained from simulations (based on the height of confined droplets measured by AFM).

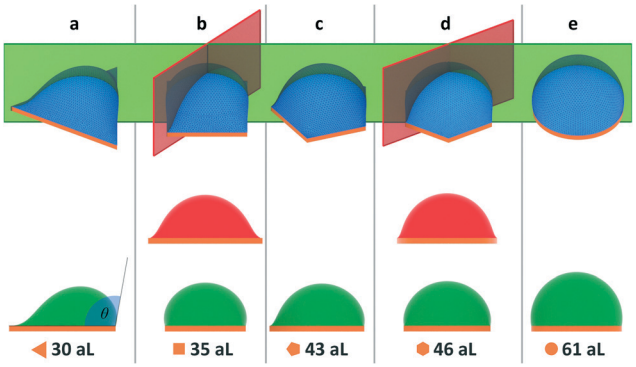

Fig. 7 Influence of the well footprint on a maximum confinable volume above the rim; from left to right: (a) 3, (b) 4, (c) 5, (d) 6 and (e) *n*-edges (footprint surface area (S_{FP}) is the same as that for the small rectangular well – 0.25 μm^2). The cross-sections defined by orthogonal and diagonal planes are shown as green and red outlines, respectively. The contact angle between the droplet and top surface measured in the middle of the rim edge (green outlines) corresponds to the wetting angle of the hydrophobic upper surface (θ = 99.7°).

for de-wetting is $\theta > (\pi + \alpha)/2$. The droplets are confined in the well if the wetting angle on adjacent vertical walls is in a range defined by the limit values for capillary self-motion and de-wetting. For instance, for an equilateral triangle (Fig. 7a) where $\alpha = 60°$, the full confinement of the droplet is achieved if the contact angle θ is in the interval 60–120°. The 'working' intervals for other shapes are as follows: square (Fig. 7b) <45–135°>, pentagon (Fig. 7c) <36–144°>, hexagon (Fig. 7d) <30–150°> and circle (Fig. 7e) <0–180°>. The non-uniformity of the contact angle along the rim circumference has significant influence on the maximum confinable volume, as presented in Fig. 7 for rectangular wells with S_{FP} = 0.25 μm^2. The maximum confinable volume for triangular wells is less than half that for circular wells with the same footprint area (Fig. 7a–e). The cross-sections, both orthogonal and diagonal, of the droplets at equilibrium, defined by a vertical plane, are also presented in Fig. 7. The sharing of the corners of the wells, *e.g.*, on a chessboard pattern, translates into a strong pinning effect, securely confining the microdroplets and providing high utilization of the available area. The pinning effect decreases with the number of well corners, therefore the possibility of well overflow and accidental mixing with adjacent droplets is the highest for ideally circular wells. It follows that, despite confining microdroplets at lower volumes than the circular wells, the rectangular ones are more robust in terms of the variations of material and geometry parameters, and thus are less prone to accidental mixing. Finally, unlike circular wells and aside from being easier to fabricate by standard lithography, the rectangular geometries offer the additional advantage of inherently pulling in the droplets which are partially deposited outside the well due to capillarity.

Conclusions

Both experimental and simulation results demonstrate that the rectangular footprint of microstructured surfaces causes significant pinning of the microdroplets to the rim corners. This phenomenon can act as a buffer against the droplet overflow outside the confining area in case of unplanned physical or chemical changes, *e.g.*, variation of temperature or elevation of the liquid due to the decrease of surface tension caused by chemical reaction or adsorption. In particular, the chessboard-like microstructured surfaces presented here can be used when the mixing of two adjacent confined droplets is undesirable, *e.g.*, micro- and nano-arrays. Moreover, despite the lack of control over the droplet localization *via* simple spray nebulizer deposition, a majority of all available wells (3 $\mu m \times 3$ μm and 1 $\mu m \times 1$ μm) were filled by fully confined droplets as a result of the heterogeneously ordered character of the micro-structures.

On the methodology front, this study has shown that the parameters of the microdroplets confined by microstructures with surface-addressable hydrophobicity can be effectively estimated by phenomenological simulations for designing the confining structures, as well as measured by AFM for the validation of the impact of the confining effects on the performance of various devices, such as micro- and nano-arrays, and lab-on-a-chip devices.

Contribution of the authors

OK performed the simulations, HZ, GRS, XB and FP-M performed the experiments, and DVN designed the microstructures and the experiments, and initiated and directed the project. All authors contributed to planning the work, data interpretation, and writing the manuscript.

Acknowledgements

This work was financially supported by joint European Commission–Australian Department of Education Science and Trade (DEST) research cooperative grants, through the FP6 Programme (FP6/2002-2006) project Charged Particle Nanotechnology (CHARPAN, under grant agreement number 15803) and through The Commonwealth of Australia under the DEST International Science Linkages Program (Grant No. CG090203), and by the Canadian Foundation for Innovation (CFI) project BioNanoFactory. We thank Dr. Udo Bach from the ARC Centre of Excellence for Electromaterials Science, Monash University, Australia for insightful discussions and the use of AFM instrumentation.

Notes and references

1 E. Gogolides, K. Ellinas and A. Tserepi, *Microelectron. Eng.*, 2015, **132**, 135–155.
2 M. S. Algahtani, D. J. Scurr, A. L. Hook, D. G. Anderson, R. S. Langer, J. C. Burley, M. R. Alexander and M. C. Davies, *J. Controlled Release*, 2014, **190**, 115–126.
3 G. McHale, *Analyst*, 2007, **132**, 192–195.
4 J. T. Smith, B. L. Viglianti and W. M. Reichert, *Langmuir*, 2002, **18**, 6289–6293.
5 Y. Zhou, O. Andersson, P. Lindberg and B. Liedberg, *Microchim. Acta*, 2004, **146**, 193–205.

 This journal is © The Royal Society of Chemistry 2016

6 E. K. Sackmann, A. L. Fulton and D. J. Beebe, *Nature*, 2014, **507**, 181–189.
7 B. Farshchian, S. Park, S. Park, J. Choi, A. Amirsadeghi and J. Lee, *Lab Chip*, 2012, **12**, 4764–4771.
8 N. Vergauwe, D. Witters, Y. T. Atalay, B. Verbruggen, S. Vermeir, F. Ceyssens, R. Puers and J. Lammertyn, *Microfluid. Nanofluid.*, 2011, **11**, 25–34.
9 R. B. Fair, *Microfluid. Nanofluid.*, 2007, **3**, 245–281.
10 Y. Fouillet, D. Jary, C. Chabrol, P. Claustre and C. Peponnet, *Microfluid. Nanofluid.*, 2008, **4**, 159–165.
11 J. K. Luo, Y. Q. Fu, Y. Li, X. Y. Du, A. J. Flewitt, A. J. Walton and W. I. Milne, *J. Micromech. Microeng.*, 2009, **19**, 054001.
12 R. Bogue, *Sens. Rev.*, 2007, **27**, 7–13.
13 J. Kim, H. Park, B. Kang, R. Ku, C. Ham and M. Yang, *J. Appl. Phys.*, 2011, **110**, 084701.
14 J. Y. Kim, K. Choi, D. I. Moon, J. H. Ahn, T. J. Park, S. Y. Lee and Y. K. Choi, *Biosens. Bioelectron.*, 2013, **41**, 867–870.
15 L. Wen, J. C. Weaver and G. V. Lauder, *J. Exp. Biol.*, 2014, **217**, 1656–1666.
16 G. S. Watson, D. W. Green, L. Schwarzkopf, X. Li, B. W. Cribb, S. Myhra and J. A. Watson, *Acta Biomater.*, 2015, **21**, 109–122.
17 G. S. Watson, S. Myhra, B. W. Cribb and J. A. Watson, *Biophys. J.*, 2008, **94**, 3352–3360.
18 A. R. Parker and C. R. Lawrence, *Nature*, 2001, **414**, 33–34.
19 W. Barthlott and C. Neinhuis, *Planta*, 1997, **202**, 1–8.
20 T. L. Sun, L. Feng, X. F. Gao and L. Jiang, *Acc. Chem. Res.*, 2005, **38**, 644–652.
21 A. Marmur, *Langmuir*, 2003, **19**, 8343–8348.
22 A. B. D. Cassie and S. Baxter, *Trans. Faraday Soc.*, 1944, **40**, 0546–0550.
23 R. N. Wenzel, *Ind. Eng. Chem.*, 1936, **28**, 988–994.
24 A. Marmur, *Soft Matter*, 2013, **9**, 7900–7904.
25 R. Seemann, M. Brinkmann, E. J. Kramer, F. F. Lange and R. Lipowsky, *Proc. Natl. Acad. Sci. U. S. A.*, 2005, **102**, 1848–1852.
26 A. Biswas, I. S. Bayer, A. S. Biris, T. Wang, E. Dervishi and F. Faupel, *Adv. Colloid Interface Sci.*, 2012, **170**, 2–27.
27 D. Fine, A. Grattoni, R. Goodall, S. S. Bansal, C. Chiappini, S. Hosali, A. L. van de Ven, S. Srinivasan, X. Liu, B. Godin, L. Brousseau, I. K. Yazdi, J. Fernandez-Moure, E. Tasciotti, H. J. Wu, Y. Hu, S. Klemm and M. Ferrari, *Adv. Healthcare Mater.*, 2013, **2**, 632–666.
28 G. S. Grest, D. R. Heine and E. B. Webb Iii, *Langmuir*, 2006, **22**, 4745–4749.
29 S. Khan and J. K. Singh, *Mol. Simul.*, 2014, **40**, 458–468.
30 A. Milchev, in *Computer Simulations in Condensed Matter Systems: From Materials to Chemical Biology Volume 2*, ed. M. Ferrario, G. Ciccotti and K. Binder, Springer Berlin Heidelberg, Berlin, Heidelberg, 2006, vol. 704, pp. 105–126.
31 J. A. Ritchie, J. S. Yazdi, D. Bratko and A. Luzar, *J. Phys. Chem. C*, 2012, **116**, 8634–8641.
32 C. Yang, U. Tartaglino and B. N. J. Persson, *Eur. Phys. J. E: Soft Matter Biol. Phys.*, 2008, **25**, 139–152.
33 G. O. Berim and E. Ruckenstein, *Langmuir*, 2006, **22**, 1063–1073.
34 A. P. Malanoski, B. J. Johnson and J. S. Erickson, *Nanoscale*, 2014, **6**, 5260–5269.
35 S. Herminghaus, M. Brinkmann and R. Seemann, *Annu. Rev. Mater. Res.*, 2008, **38**, 101–121.
36 H. Gau, S. Herminghaus, P. Lenz and R. Lipowsky, *Science*, 1999, **283**, 46–49.
37 P. Lenz and R. Lipowsky, *Phys. Rev. Lett.*, 1998, **80**, 1920–1923.
38 M. Brinkmann and R. Lipowsky, *J. Appl. Phys.*, 2002, **92**, 4296–4306.
39 C. Priest, R. Sedev and J. Ralston, *Colloid Polym. Sci.*, 2013, **291**, 271–277.
40 A. Méndez-Vilas, A. B. Jódar-Reyes and M. L. González-Martín, *Small*, 2009, **5**, 1366–1390.
41 A. Marmur, *Langmuir*, 1993, **9**, 1922–1926.
42 S. Herminghaus, T. Pompe and A. Fery, *J. Adhes. Sci. Technol.*, 2000, **14**, 1767–1782.
43 N. Ishida, T. Inoue, M. Miyahara and K. Higashitani, *Langmuir*, 2000, **16**, 6377–6380.
44 J. Geerlings, E. Sarajlic, J. W. Berenschot, R. G. P. Sanders, L. Abelmann and N. R. Tas, *2014 IEEE 27th International Conference on Micro Electro Mechanical Systems (MEMS)*, 2014, pp. 100–103, DOI: 10.1109/MEMSYS.2014.6765583.
45 A. Gunning, A. Mackie, P. Wilde and V. Morris, *Langmuir*, 2004, **20**, 116–122.
46 X. H. Zhang and W. Ducker, *Langmuir*, 2008, **24**, 110–115.
47 A. Checco, H. Schollmeyer, J. Daillant, P. Guenoun and R. Boukherroub, *Langmuir*, 2006, **22**, 116–126.
48 A. Meister, M. Liley, J. Brugger, R. Pugin and H. Heinzelmann, *Appl. Phys. Lett.*, 2004, **85**, 6260–6262.
49 A. Méndez-Vilas, A. B. Jódar-Reyes and M. L. González-Martín, *Small*, 2009, **5**, 1366–1390.
50 F.-I. Li, P. H. Leo and J. A. Barnard, *J. Phys. Chem. C*, 2008, **112**, 14266–14273.
51 A. Bauer, P. McGlynn, L. L. Bovet, P. L. Mims, L. A. Curry and J. P. Hanrahan, *Respir. Care*, 2009, **54**, 1342–1347.
52 M. B. Dolovich, R. C. Ahrens, D. R. Hess, P. Anderson, R. Dhand, J. L. Rau, G. C. Smaldone and G. Guyatt, *Chest*, 2005, **127**, 335–371.
53 I. Horcas, R. Fernandez, J. M. Gomez-Rodriguez, J. Colchero, J. Gomez-Herrero and A. M. Baro, *Rev. Sci. Instrum.*, 2007, **78**, 013705.
54 K. A. Brakke, *Philos. Trans. R. Soc., A*, 1996, **354**, 2143–2157.
55 T. H. Chou, S. J. Hong, Y. J. Sheng and H. K. Tsao, *Langmuir*, 2012, **28**, 5158–5166.
56 Y. Chen, B. He, J. H. Lee and N. A. Patankar, *J. Colloid Interface Sci.*, 2005, **281**, 458–464.
57 S. Brandon, N. Haimovich, E. Yeger and A. Marmur, *J. Colloid Interface Sci.*, 2003, **263**, 237–243.
58 W. H. Hager, *J. Hydraul Res.*, 2012, **50**, 3–9.
59 N. R. Pallas and Y. Harrison, *Colloids Surf.*, 1990, **43**, 169–194.
60 K. A. Brakke, *Exp. Math.*, 1992, **1**, 141–165.
61 C. A. Schneider, W. S. Rasband and K. W. Eliceiri, *Nat. Methods*, 2012, **9**, 671–675.
62 A. F. Stalder, G. Kulik, D. Sage, L. Barbieri and P. Hoffmann, *Colloids Surf., A*, 2006, **286**, 92–103.
63 P. Concus and R. Finn, *Proc. Natl. Acad. Sci. U. S. A.*, 1969, **63**, 292–299.
64 J. Berthier and K. A. Brakke, *The physics of microdroplets*, John Wiley & Sons, Inc., Hoboken, NJ, 2012.

This journal is © The Royal Society of Chemistry 2016

Electronic Supplementary Material (ESI) for Lab on a Chip.
This journal is © The Royal Society of Chemistry 2016

Supporting Information

Confinement of Water Nanodroplets on Rectangular Micro/Nano-arrayed Surfaces

Ondřej Kašpar,[1,#] *Hailong Zhang,*[2,#] *Viola Tokárová,*[1] *Reinhard I. Boysen,*[2] *Gemma Rius Suñé,*[3] *Xavier Borrise,*[3] *Francesco Perez-Murano,*[3] *Milton T. W. Hearn,*[2] *Dan V. Nicolau,*[1,2,*]

For better understanding the main workflow of this study is shown in **Scheme S1**. Figures 3, 4 and 5 are based purely on simulation results, Figure 6 represents comparison of experimental data - CA_AFM and simulation - CA_sim(h_AFM).

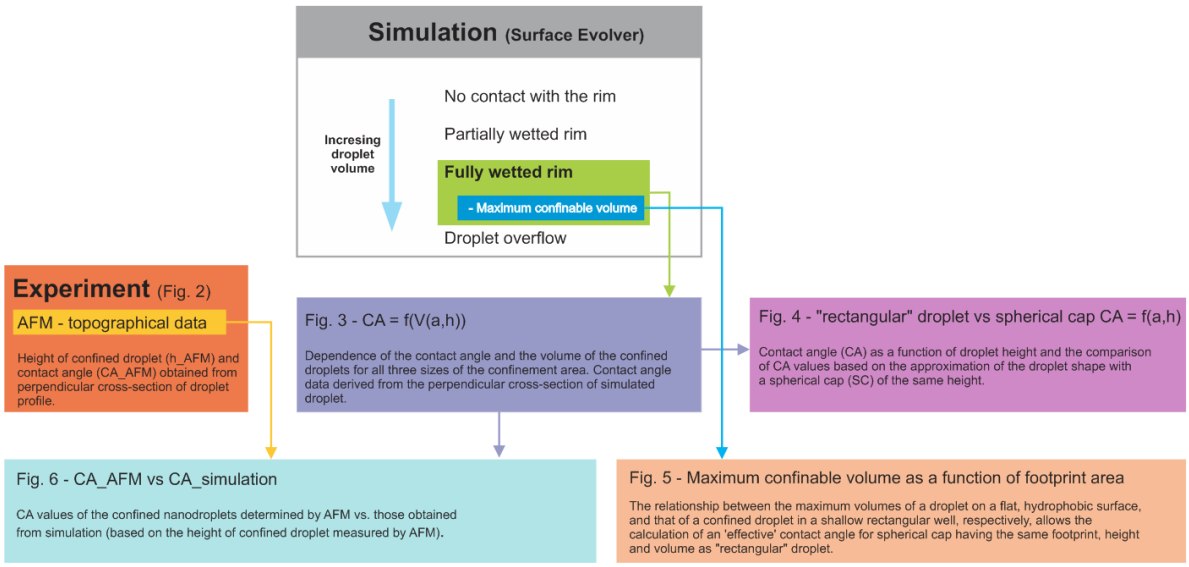

Scheme S1. Experimental and Simulation workflow

S1 Design and fabrication of micro/nano-structured array

The micro-structured arrays were manufactured on 1 x 1 cm^2 chips cut from P-doped silicon wafers submitted to a dry thermal oxidation process to form a 40 nm thick SiO_2 layer. The chessboard-like organized, 50 × 50 μm^2 patterned areas, with squares with the x/y-dimensions of 0.5 µm (small), 1 µm (medium) and 3 µm (large), were defined by e-beam lithography and two different post-processing sequences (described in **Figure S1**), resulting in three types of structures: A, B, and C (**Table S1**).

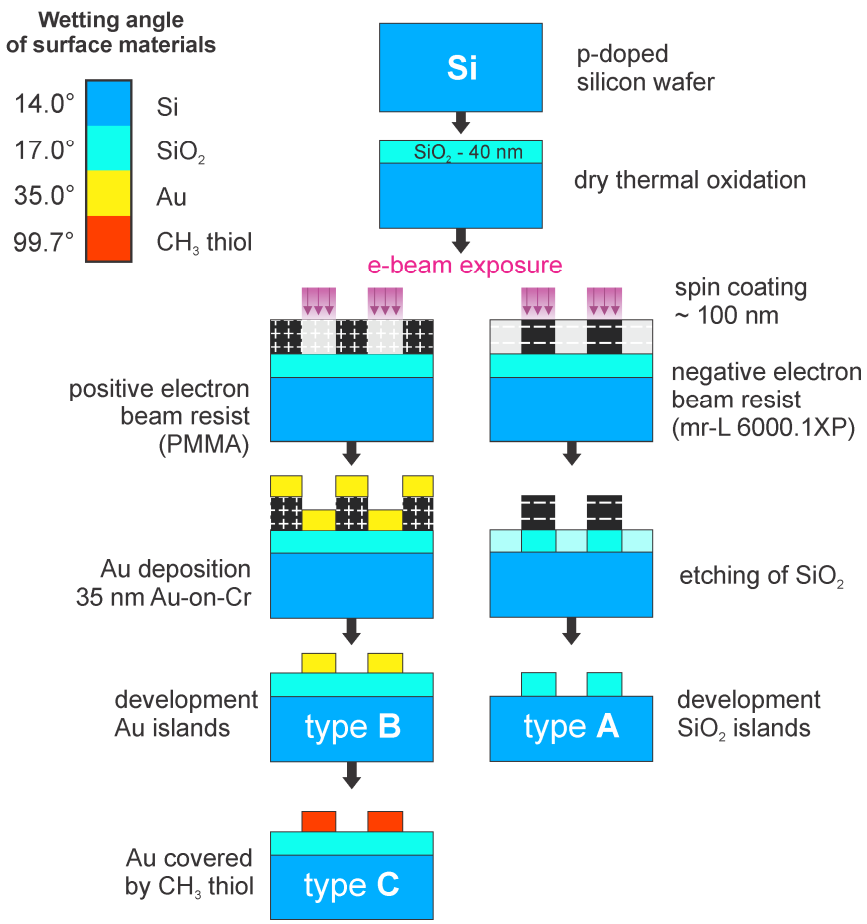

Figure S1. Step-by-step fabrication of droplet confining structures

Table S1. Heterogeneous structures - combination of top and basal substrates

Top / Basal	**SiO_2** (17°)	**Au** (35°)	**CH_3 thiol** (99.7°)
Si/ SiO_2 (14 - 17°)	Type A	Type B	Type C

Note: The contact angle of materials is indicated in the top row and left column, for the top and basal materials, respectively.

S1.1 Structure Type A (SiO_2-on-Si)

A 100 nm thick layer of a negative electron beam resist (mr-L 6000.1XP from MicroResist Technology GmbH, Germany) was deposited by spin coating on top of the oxidized silicon chip and then subjected to e-beam lithography. After development, the remaining cross-linked resist serves as a mask for the SiO_2 etching. Wet etching was performed by immersing the chip in a buffered HF solution (SiO_2 etching solution, Merck, Germany) for 20 sec. to selectively etch 40 nm of SiO_2 layer. After the wet etching the resist was eliminated by pyrolysis at 600 ºC in the O_2 environment for 5 minutes. The process has been fully described and characterized elsewhere.[1]

S1.2 Structure Type B (Au-on-SiO_2)

A 100 nm thick layer of a positive electron beam lithography resist (poly-methyl methacrylate, PMMA 950k) was deposited by spin coating on top of the oxidized silicon chip and then subjected to e-beam lithography and development to locally remove the PMMA to form a chessboard pattern; a 35nm thick gold-on-chromium (30 nm/5 nm) layer was deposited over the whole chip

by e-beam evaporation; the remainder of PMMA was removed with acetone resulting in an oxidized silicon surface interrupted by gold protrusions.

S1.3 Structure Type C (CH_3 thiol-on-Si)

The structures Type C present bare silicon (hydrophilic) as basal layer and methyl-terminated thiol-functionalized Au (hydrophobic) as elevated layer. These structures have been investigated in the greatest detail.

S2 Droplet simulations

The shape of the droplet confined in rectangular wells has been simulated using Surface Evolver, a public domain software.[2] Surface Evolver program, which has been extensively used to analyze the fluid interface,[3] calculates the shape of a droplet at equilibrium, through the minimization of the free energy of the system. At the micro-scale, the capillary and surface tension forces are predominant compared with gravity. The equilibrium shape of the droplet has been obtained iteratively from the initial shape, e.g., a box, positioned into a fixed model of the well as showed in **Figure S2a**. The process was divided into a series of individual steps to ensure stable simulations (**Figure S2b-d**). After each iteration step the vertices on the interface were moved to reduce the energy of the system while adhering to set of imposed constraints. Detailed information about the software, syntaxes and principles are available in the Surface Evolver manual.[4] The contact angle was measured by a public domain software, ImageJ,[5] with implemented plugin that had been designed especially for the drop shape analysis – DropSnake.[6]

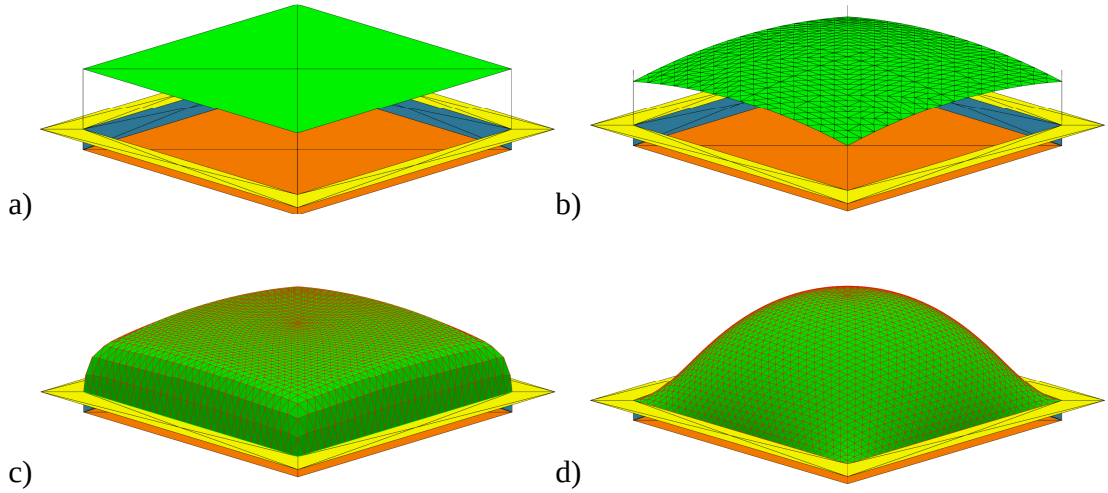

Figure S2. The evolution of the droplet shape in a well Type C (small): a) Initial configuration - green box (dematerialized for better visibility) represents a constant volume of the droplet in the well defined by the bottom (orange) and the walls (dark blue) b) evolution of the droplet in a well of an infinite height c) application of constrains to ensure rim wetting (yellow) d) equiangulation and vertex averaging of the surface has been followed by 2000 iteration steps.

S3 Experimental results

Effect of chemically heterogeneous surface properties

The Type A micro-structured surfaces present only a very small difference between the hydrophilicity of the basal (Si) and top layer (SiO_2), i.e., approximately 3º, which is within the measurement error. Even for this surface, with near-perfect homogenous physico-chemistry, the nm-range topography had a sizable impact on the confinement of the water micro-droplets (**Figure S3a**). While there are small water 'residues' on the top surface, essentially all droplets with sizes significantly smaller that the edge of the micro/nano-well are confined within the well, with a clear preference for wetting trilateral surfaces, i.e., corners and edges of the well. The Type

B micro-structured surfaces, with differences between the contact angle for their top and basal surfaces of 21°, induce similar 'corner wetting' behavior as the Type A surfaces, but only for larger droplets, i.e., those with a footprint similar with, or larger than the confining rectangular wells (**Figure S3b**). Smaller droplets as confined by smaller wells exhibit a behavior more similar to that observed on micro-structured surfaces with larger differences in local hydrophobicity (Type C). The SAM-modified micro-structures with high differences between the hydrophobicity on the top and on the basal surface induced large differences in the wetting behavior of the water micro-droplets. Specifically, the micro-droplets are nearly perfectly confined on the hydrophilic bottom of the wells surrounded by highly hydrophobic CH_3-thiol functionalized terminated Au walls (surface Type C, **Figure S3c**). The Type C has been therefore chosen as model chemically- and topographically- heterogeneous structure with ability to confine micro-droplets.

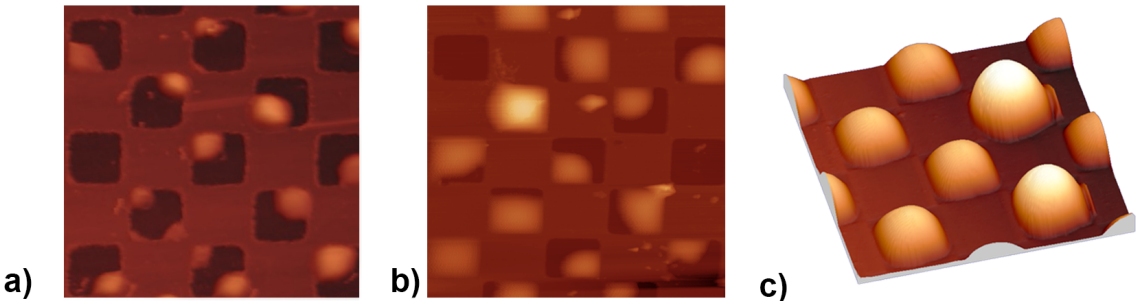

Figure S3. Dependence of the behavior of micro-droplets by spatially addressable hydrophobicity (3 µm × 3 µm). The confining topography can ensure the confinement of droplets for nearly-even hydrophilic surfaces (a: Type A), but only for small droplets, which are wetting the corners (low energy configuration). Structures with moderate differences in the local hydrophobicity (b: Type B) shows similar behavior as the Type A, but only for larger droplets. The micro-structures with large differences in the local hydrophobicity, with hydrophilic basal surface and hydrophobic walls and rim (c: Type C) ensure a near-perfect confinement.

Simulation and analysis

It has been shown that in the case of a rectangular well, the stability and shape of a droplet is highly affected by the wall properties, described as Concus-Finn relations.[7] If the wetting angle θ of the wall in rectangular well is smaller than 45°, the liquid tends to form a wedge and spread along the edges, eventually outside the rim, resulting in poor confinement of the droplet. Condition for capillary self-motion is

$$\theta < \frac{\pi}{2} - \alpha \,, \qquad \textbf{(Equation S1)}$$

where θ – the Young contact angle on both adjacent planes, α – the wedge half-angle (for rectangular well $\alpha = \pi/4$). On the other hand, if the contact angle is higher than 135°, the droplet detaches and the edge is no longer wetted:

$$\theta > \frac{\pi}{2} + \alpha . \qquad \textbf{(Equation S2)}$$

According to the Concus-Finn relation in the case of well Type A, and B droplet preferably wets corners. If the gravity force is neglected, the droplet has tendency to rise along the edges of the well and spread on the hydrophilic rim. The near-perfect confinement properties of the well Type C (**Figure S3b**) was further rigorously studied by the Surface Evolver software. The example of a steady droplet for the well Type C is shown in **Figure S4**.

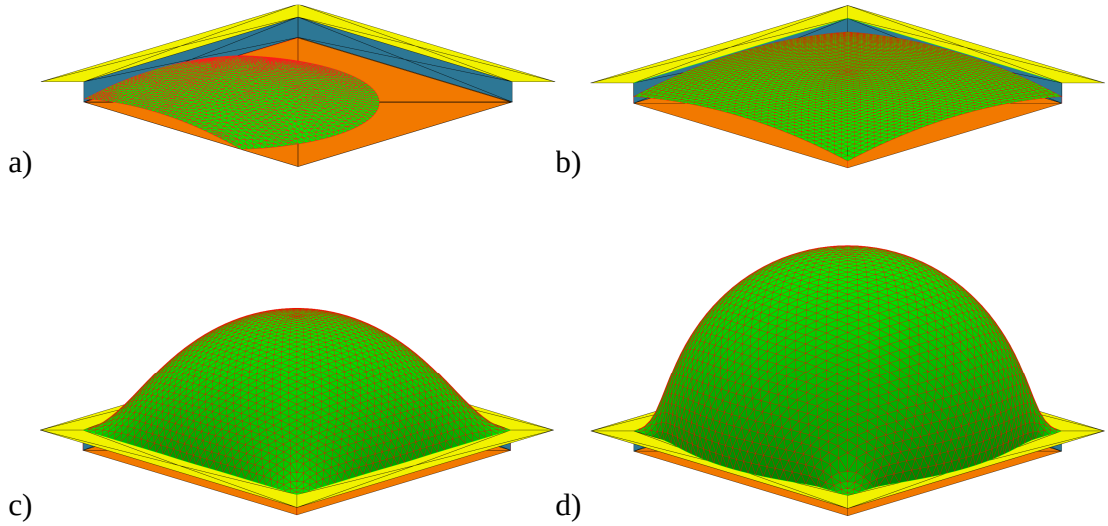

Figure S4. Droplet volume vs. shape for the well Type C (small); a) wetting of one bottom corner; b) complete bottom wetting, no contact with the rim (yellow); c) maximal possible volume of the droplet, no wetting of the rim; d) overflow of the liquid on the rim

The droplet of a small volume can either wet one, or more corners of the well, as presented in **Figure S4a**. The position of the contact line depends on a wettability difference between the bottom and the wall of the well. From theory, if θ_{wall} - θ_{bottom} > π/2 the contact line merges with the well bottom edge and droplet whole volume sits only on the hydrophilic bottom of the well.[8] In our case, the difference $\Delta\theta$ for Type C is 82.7° and contact line is therefore located on the wall (**Figure S4a**). Another possible conformation is a small droplet sitting on the bottom of the well without physical contact with the walls. Larger volumes of the droplet causes complete wetting of the bottom, and eventually contact with the rim, as presented in **Figure S4b**. The contact line is pinned from the middle of the edge until the whole rim circumference is in a contact with the droplet surface (**Figure S4c**). Additional volume results in decreasing the curvature radius until the fluid overflows on the rim (**Figure S4d**). This behavior can be explained by the non-uniform

contact angle along the rectangular well. The two main cross-sections were investigated and are presented in **Figure S5**.

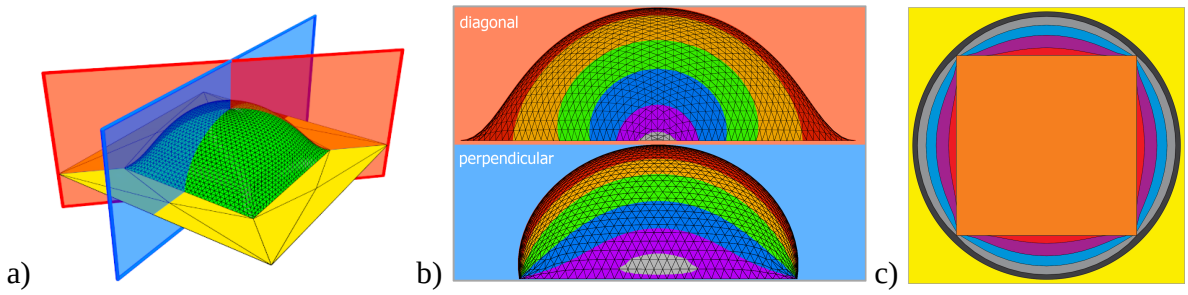

Figure S5. Contact angle variability along the contact line in rectangular well (Type C) – a) 3D visualization - the red plane shows the diagonal cross-section, the blue plane represents the perpendicular cross-section; b) decrease of the droplet curvature radius towards the well corner – red; and towards the rim edge - blue (individual colored areas represent parallel cross-sections); c) bottom view - contact lines of overflowed droplet on the well rim (orange square represents footprint of the well)

The red diagonal cross-section shows inflection point in the proximity of the rim corner and the contact angle is hardly determined. The contact angle value of the droplet in rectangular well was determined from the blue, perpendicular cross-section. Parallel diagonal cross-sections show the decrease of the droplet curvature radius towards the rim corner (**Figure S5b**). This phenomenon causes an increase of the Laplace pressure in the proximity of the rim corner. Liquid is consequently forced to spread towards the center of rim edge and eventually overflows on the top of well rim (**Figure S5c**).

A more detailed relationship between the droplet volume and the contact angle of the rim for well Type C (small) is presented in **Figure S6**. The contact angle shows an exponential growth from its initial value of 9.7° (99.7° - π/2) to 99.7°. Droplet of very small volume (V < 7.5 aL) can either sit on the bottom of the well or in one or more corners as described above. An increase of the volume causes wetting of adjacent walls (blue outline) followed by partial and complete wetting of the rim (green outline). At this point the contact angle between droplet and rim (horizontal plane) can be determined. A further increase of droplet volume leads to increase of the contact angle (CA) value to the point when CA reaches CA of the rim material and no more addition is possible to avoid droplet overflow (red outline). If the maximal confined volume is exceeded droplet overflows on the rim in the middle of rim edge but at the same time remains pinned in the rim corners (black outline) as showed in **Figure S6**.

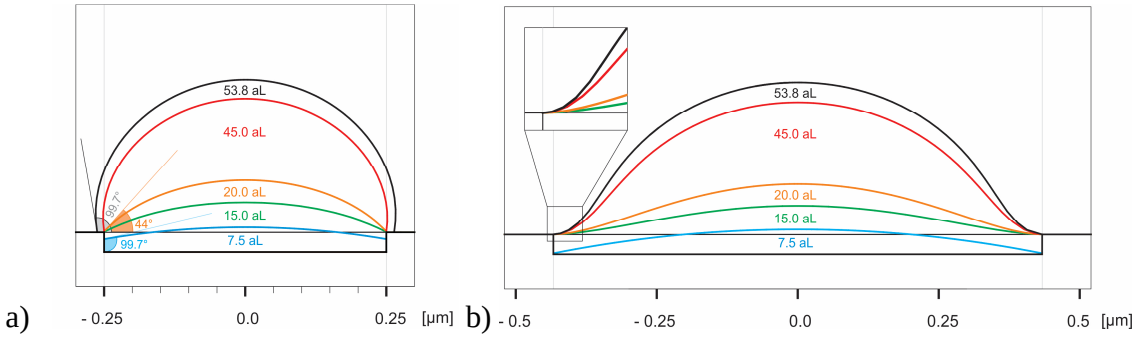

Figure S6. Droplet volume vs. contact angle for well Type C (small) – a) perpendicular cross-section b) diagonal cross-section – zoomed area shows inflection point

The results of the contact angle as a function of a droplet volume measurement are summarized in the **Figure S7**. The "critical" points when the droplet partially or fully wets the rim and when it reaches the maximum and overflow the rim are labelled in different shades of grey.

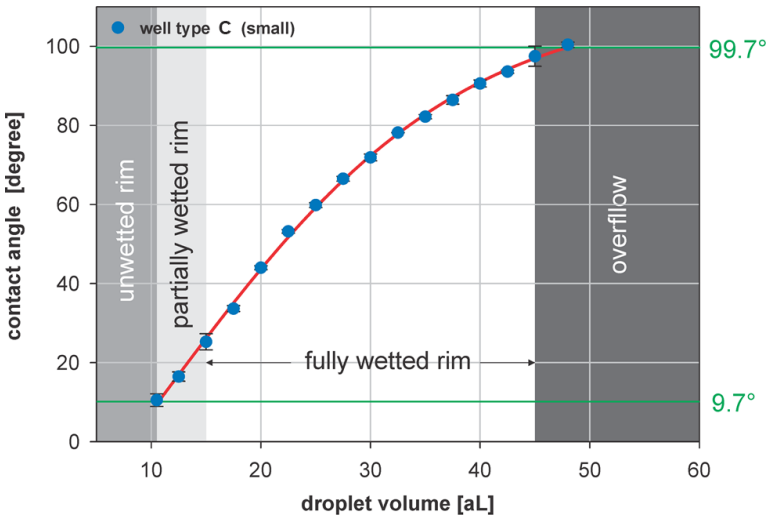

Figure S7. Dependence of contact angle as a function of droplet volume for well Type C (small)

Note: The value of contact angle is determined from the perpendicular cross-section of the simulated droplet shape; the contact angle is measured between droplet and the horizontal rim of the well

The height of confined droplet measured by the AFM was chosen as the most reliable parameter to determine CA value by Surface Evolver simulation. The results obtained from the simulation are shown in **Figure S8**. Dependence of the contact angle on droplet height, for all three size classes of the well Type C, is described by a 3-parametric non-linear regression equation $CA_{sim} = y_0 + a.x^b$, where CA_{sim} is a contact angle obtained from the simulation, x is the height of the droplet and y_0, a and b are regression coefficients. This equation has been chosen as the best approximation for relatively complex shape of rectangular droplet.

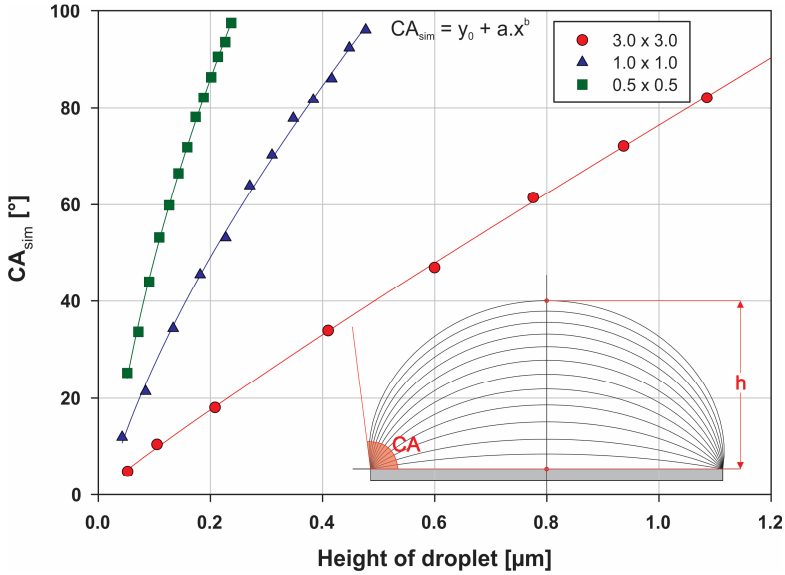

Figure S8. Dependence of the droplet height on CA_{sim} obtained from the simulation (measured in the perpendicular cross-section of the well)

The rectangular character of the footprint results in the non-uniformity contact angle along the rim contact line and affects maximal volume of the confined droplet. Maximal volume of the droplet above the rim (without the base) for circular well with the same footprint area is 1.69-times higher than that of the rectangular one (61.25 aL and 36.25 aL for small C well, respectively) as shown in **Figure S9**.

a) 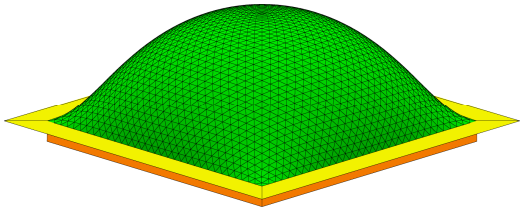 b) 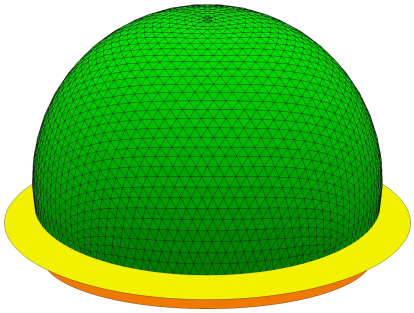

Figure S9. Maximal confined droplet shape and volume for the same footprint area of a) rectangular foot-print (volume of the droplet above the rim - 36.25 aL), b) circular foot-print (volume of the droplet above the rim - 61.25 aL)

References

[1] C. Martin, G. Rius, A. Llobera, A. Voigt, G. Gruetzner, F. Perez-Murano, Microelectron Eng 2007, 84, 1096.

[2] K. A. Brakke, Exp Math 1992 , 1, 141.

[3] T. H. Chou, S. J. Hong, Y. J. Sheng, H. K. Tsao, Langmuir 2012, 28, 5158; Y. Chen, B. He, J. H. Lee, N. A. Patankar, J Colloid Interf Sci 2005, 281, 458; S. Brandon, N. Haimovich, E. Yeger, A. Marmur, J Colloid Interf Sci 2003, 263, 237.

[4] K. A. Brakke, Surface Evolver documentation 2013, can be found under: http://www.susqu.edu/facstaff/b/brakke/evolver.

[5] C. A. Schneider, W. S. Rasband, K. W. Eliceiri, Nat Methods 2012, 9, 671.

[6] A. F. Stalder, G. Kulik, D. Sage, L. Barbieri, P. Hoffmann, Colloid Surface A 2006, 286, 92.

[7] P. Concus, R. Finn, Proceedings of the National Academy of Sciences 1969, 63, 292.

[8] K. A. Brakke, J Geom Anal 1992, 2, 11.